




828 kHz retinal imaging with an 840 nm Fourier domain mode locked laser

MARIE KLUFTS,¹ ALEJANDRO MARTÍNEZ JIMÉNEZ,² SIMON LOTZ,¹ MUHAMMAD ASIM BASHIR,¹ TOM PFEIFFER,³ ALEXANDER MLYNEK,³ WOLFGANG WIESER,³ ALEXANDER CHAMOROVSKIY,⁴ ADRIAN BRADU,²  ADRIAN PODOLEANU,²  AND ROBERT HUBER^{1,*} 

¹*Institute of Biomedical Optics, University of Lübeck, Lübeck 23562, Germany*

²*School of Physical Sciences, University of Kent, Canterbury CT2 7NH, United Kingdom*

³*Optores GmbH, Munich, 80339, Germany*

⁴*Superlum Diodes Ltd., Carrigtwohill, Cork T45 FC93, Ireland*

**robert.huber@uni-luebeck.de*

Abstract: This paper presents a Fourier domain mode locked (FDML) laser centered around 840 nm. It features a bidirectional sweep repetition rate of 828 kHz and a spectral bandwidth of 40 nm. An axial resolution of ~ 9.9 μm in water and a 1.4 cm sensitivity roll-off are achieved. Utilizing a complex master-slave (CMS) recalibration method and due to a sufficiently high sensitivity of 84.6 dB, retinal layers of the human eye in-vivo can be resolved during optical coherence tomography (OCT) examination. The developed FDML laser enables acquisition rates of 3D-volumes with a size of $200 \times 100 \times 256$ voxels in under 100 milliseconds. Detailed information on the FDML implementation, its challenging design tasks, and OCT images obtained with the laser are presented in this paper.

© 2023 Optica Publishing Group under the terms of the [Optica Open Access Publishing Agreement](#)

1. Introduction

With the aim of studying human tissue in-vivo, OCT is mainly used in medical fields where a non-contact method is preferred since it can generate non-invasive depth-resolved images with micrometer resolution [1]. For instance, OCT is highly valued in ophthalmology because it can resolve retinal structures in-vivo non-invasively and contact-free [2]. Most OCT systems on the market are based on spectral-domain OCT (SD-OCT) [2]. It has proven its ability to distinguish retinal layers with ~ 5 μm axial resolution and ~ 100 dB sensitivity [3–6]. These SD-OCT systems mainly operate at a center wavelength of 850 nm rather than in the 1050 nm range, which is more standard for swept-source OCT (SS-OCT) systems. One reason is that SD-OCT usually uses silicon-based line scan cameras. Also, 850 nm is a long enough wavelength to be in the non-visible region, allowing comfortable viewing during eye examinations. Low water absorption, better transversal resolution, and better axial resolution at shorter wavelengths for the same bandwidth are other reasons for the interest in 850 nm devices compared to 1050 nm.

In flying-spot technologies (where the laser beam scans the sample pixel by pixel), SD-OCT setups are limited in terms of speed by the readout time of the camera sensor. Different alternatives have been used to overcome this limitation, such as using multiple spectrometers and cameras [7]. However, these implementations require complex and more expensive systems. Regarding non-flying-spot, full-field OCT has progressed in volume rate by illuminating and acquiring the data of the whole sample in one single shot. This way, 1 kHz volume rates can be obtained [8]. This high speed however, induces a decrease in the system's sensitivity due to shorter integration times. Crosstalk between different pixels caused by multiple scattering [9] might also corrupt full-field images if not corrected like in [10]. Additionally, in such systems, balanced

detection to suppress the noise of the light source is more difficult to implement due to the need to secure pixel-to-pixel correspondence between two 2D cameras. This is not an issue for SS-OCT. SS-OCT is more attractive due to its simplified set-up that can also achieve high volume rates (400 Hz) without impacting the sensitivity [11,12]. Performances of SS-OCT depend principally on the wavelength tunable light source used for imaging. Most ophthalmic systems using swept sources take advantage of the better penetration depth in choroid at 1060 nm. At this wavelength, the water absorption exhibits a local minimum that allows for high-quality imaging and deeper penetration because of lower scattering at longer wavelengths [13–18]. However, 1060 nm OCT images often yield lower contrast in the upper retinal layers compared to 850 nm systems. Additionally, in the 1060 nm band, it is difficult to increase the axial resolution further than ~ 4 μm due to water absorption [19,20]. Shorter wavelength swept sources would not be limited in bandwidth by the water absorption and better transverse resolution can be achieved, making them interesting for studying the human retina [1,21–24]. Although imaging at shorter wavelengths is attractive for the reasons mentioned above, 850 nm SS-OCT of the human retina in vivo has only been reported at moderate speeds [25–28]. This is due to several challenges (detailed in the following section) in implementing 850 nm swept sources compared to sources at 1060 nm.

Several 850 nm swept sources have already been demonstrated with different performances. Some with a high A-Scan rate, like at 90.9 MHz using a photonic time stretch laser but at reduced sensitivity (45 dB) [29]. An A-scan rate of 998.5 kHz has been demonstrated using akinetic operation dispersion tuning and dual-mode locking [30], but at decreased axial resolution (4 nm bandwidth) and imaging range (1 mm). Different vertical-cavity surface-emitting lasers (VCSELs) have also been presented. Some with thermal tuning of a micro-electromechanical system (MEMS), which limits the repetition rates to 0.70 kHz [31,32], or one based on current modulation achieving a sweep rate of 50 kHz with a tuning bandwidth of 4.5 nm and a sensitivity roll-off of -3 dB at more than 2.5 cm [26]. Faster VCSELs have been developed using an electrically pumped MEMS, enabling a tuning bandwidth of over 37.7 nm at a frequency of 350-430 kHz [33]. Fabry-Pérot filters (FFP-TF) are used in other demonstrations [27,34], and have shown promising results. These lasers demonstrate good axial resolution but a low repetition rate due to the filter's maximal 1 kHz driving frequency. External cavity tunable filters can also give good performance regarding axial resolution (~ 7 μm) and sensitivity (96 dB) [28], as well as polygon scanner setups with a sensitivity above 90 dB and a 10 μm axial resolution [25,35,36]. 840 nm swept sources currently manufactured by Exalos Inc. and Superlum Ltd. have a wide bandwidth of over 60 nm but have a limited repetition rate of 20 kHz and ~ 2 kHz, respectively. Chen & al. demonstrated retinal images using an 845 nm swept source with a repetition rate of 30 kHz but a limited coherence length of ~ 2 mm [25].

Fourier domain mode locked (FDML) lasers (design detailed in section 2) are, on the other hand, favored for their long coherence length - besides their high sweep rates [37,38]. Thanks to their long fiber cavity, a complete sweep is optically “stored” in the laser for several hundreds of roundtrips, improving the coherence of the laser. However, to enable a good phase matching of the modes during each sweep and the spectral window of the FFP-TF, the chromatic dispersion inside the laser cavity must be minimized, as explained in [39–43]. As mentioned above, FDML lasers are also well-known for their high speed and ability to reach multi-MHz sweep rates, which is important for reducing the impact of motion artifacts [44,45]. Recently, a 13.4 MHz FDML laser using optical buffering has been reported at CLEO-Europe-2023. FDML lasers are currently manufactured at 1060 nm, 1300 nm, and 1550 nm for different applications like skin and ophthalmic imaging [15,46–48], stimulated Raman spectroscopy [49], or are being used for instance in elastography for brain cancer thanks to their high phase stability [50]. Their high sweep rate has also enabled non-linear imaging at high frame rates using Spectro-temporal encoding instead of inertial scanning [51,52]. As research devices, FDML lasers have also been reported at 1200 and 1400 nm at CLEO-Europe-2023. Recently, the improved performance

of semiconductor optical amplifiers (SOAs) around 840 nm opened the door for developing an FDML laser at 840 nm [53]. This wavelength brings up new challenges like high loss in optical components, lower SOA gain and higher chromatic dispersion.

This paper focuses on the development steps of the laser. A thorough characterization of the performance parameters is presented, along with the challenges overcome to achieve FDML operation at this wavelength. Since an important application of the laser might be retinal OCT, we lay a special emphasis on the performance characterization of parameters relevant to OCT and included preliminary images.

2. 840 nm FDML laser

2.1. Challenges

In FDML lasers, spectral filtering is obtained using an FFP-TF whose driving frequency matches the inverse round-trip time of the light circulating in the cavity. A fiber spool optically stores and delays the sweep to obtain a sweep frequency around the resonance frequency of the FFP-TF, which is in our case 2×414 kHz. Due to the ~ 500 m long fiber cavity, chromatic dispersion is significant and must be compensated for good performance as mentioned previously [39–43]. To ensure a remaining chromatic delay below ~ 200 fs like in [41], a chirped fiber Bragg grating (cFBG) is used, designed to compensate for the dispersion at best inside the cavity. To guarantee the best performance of cFBGs, an accurate chromatic dispersion measurement set-up was assembled in a previous work to measure the fiber's dispersion used in the laser at the wavelength of interest [54]. The measurements have been performed around 850 nm for Hi780 fibers and around 1080 nm for Hi1060 fibers. We measured that the 1st order dispersion is three times higher around 850 nm than at 1060 nm, -100.2 ps·nm⁻¹·km⁻¹ and -33.7 ps·nm⁻¹·km⁻¹ respectively. Manufacturers of cFBGs are generally limited by the length of their phase masks, achieving a maximal compensation of $\sim 1,200$ ps. This may highly restrict the bandwidth of cFBGs. For instance, if one wants to compensate with only one cFBG the whole chromatic dispersion present in 500 meters of Hi780, the bandwidth will be 24 nm at most. To avoid this limitation, several cFBGs can compensate each a fraction of the dispersion. However, each cFBG requires a circulator. Circulators at 840 nm introduce polarization mode dispersion (PMD) and loss, which should be avoided if possible. Due to the birefringence of the internal crystal of a circulator and other effects, both axes of the light can experience different path lengths leading to modulations in the spectrum. Several experiments have been tested to investigate and quantify the PMD [53]. Theoretically, PMD can be compensated by aligning the light with one axis of the circulator using polarization controllers. However, due to the use of cFBGs, the PMD becomes wavelength dependent, complicating the compensation. Several ideas have been put forward, using for instance, a custom polarization controller or a polarization-maintaining (PM) 780 patch cord. Unfortunately, the idea of using several circulators makes these solutions not usable due to higher frequency PMD. PM-circulators could be used, but they increase the loss in the laser, which is undesirable. Semiconductor optical amplifiers (SOAs) available at 840 nm have low small signal gain (~ 22 dB), which implies that further loss should be avoided as much as possible to enable lasing.

2.2. FDML set-up description

Figure 1 shows a schematic diagram of the 840 nm FDML laser. It uses three cFBGs to enable compensation of the chromatic dispersion over a large bandwidth of 72 nm. Each cFBG compensates for a third of the total dispersion introduced by the ~ 500 m fiber spool. Circulators enable the use of cFBGs by routing the backscattered light from the cFBG with 90% reflectivity, to the following optical components in the laser cavity. Polarization controllers are placed at each circulator input to manage PMD and optimize for maximum optical power and bandwidth. An

SOA with a small signal gain of 22 dB is used in this setup as a gain medium (SOA_1, Superlum Ltd., SOA-372-DBUT-SM). An isolator is added at the input of the SOA_1 to prevent parasitic lasing that could arise from a low isolation loss of the last circulator. A 90/10 coupler is used as a monitoring port to monitor the power circulating in the cavity in order to avoid going above the catastrophic optical damage (COD) threshold of the SOA_1. Several components have been spliced together to limit the overall amount of losses in the laser cavity to 19 dB. The laser's output is directed towards a booster stage, which increases the output power from 1.7 mW to 17 mW. Due to the use of a PM-SOA (SOA_2) as an amplifier, an in-line polarizer in series with a PM-circulator is used to reduce the PMD introduced by the booster stage.

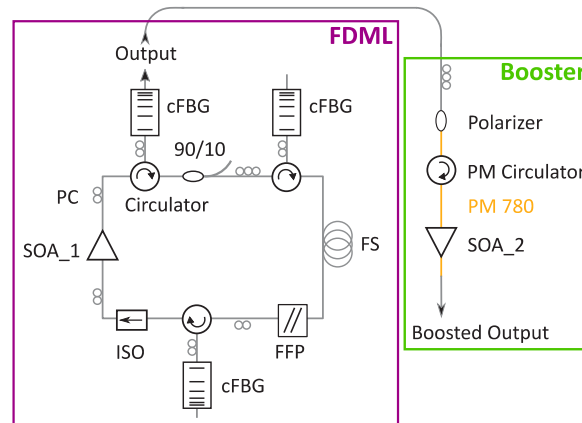


Fig. 1. FDML laser set-up accompanied by its booster stage. SOA: semiconductor optical amplifier, PC: polarization controller, cFBG: chirped fiber Bragg grating, ISO: isolator, FS: fiber spool, FFP: fiber Fabry-Pérot filter.

2.3. Laser characterization

The spectrum at the output of the 840 nm FDML laser and at the output of the booster stage are shown in Fig. 2. A tuning bandwidth of 40 nm full width at half maximum is achieved in both cases. A wider bandwidth can be achieved, however as the gain shape of the SOA_2 in the booster section (Superlum Ltd., SOA-372-PM) drops significantly with increasing distance from the gain maximum, the bandwidth achieved at -3 dB will be narrower.

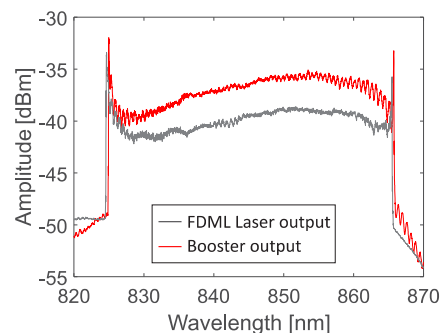


Fig. 2. Spectra at the FDML laser output in grey and at the booster stage output in red after a passing through an isolator and a coupler.

The spectral shapes exhibit ripples. Despite using PM components, they are more pronounced after the booster output (red) than in the FDML cavity (grey). The in-line polarizer cannot cancel the ripples over the entire range because of the wavelength dependency of the PMD. Although ripples and a drop of intensity in the short wavelength of the spectrum, the coherence length at 1.4 cm decreases by 6 dB only, as shown in Fig. 3. This corresponds to a frequency of ~ 700 MHz. The measurements have been performed using a Mach-Zehnder interferometer, a 40 GS/s, 20 GHz oscilloscope (Lecroy Teledyne, Wavemaster 820Zi-b), and a 23 GHz balanced photodetector (Optilab, BPR-23-M). The recalibration of each optical path difference (OPD) uses the inverted phase of the fourth (light green) OPD obtained using a Hilbert function. Before extracting the phase of the fourth OPD, a low-pass filter is applied to its interference (sampling frequency: 40 GHz, cut-off: 400 MHz). After recalibration of the phase, an FFT is performed, and all peaks are plotted together. Both sweeps, backward (decreasing wavelength) and forward (increasing wavelength) show the same roll-off.

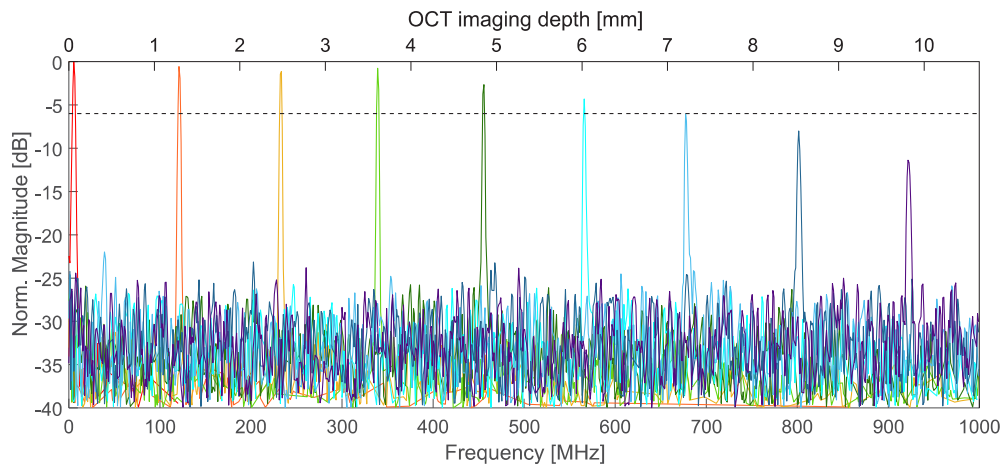


Fig. 3. Sensitivity roll-off. An OCT imaging depth of ~ 7 mm corresponding to a frequency of 700 MHz can be approximated. Calibration is effectuated using the fourth (light green) optical path difference.

The noise of the laser has also been studied at the output of the laser, as shown in Fig. 4. A low-pass filter is applied to the signal in post-processing (sampling frequency: 40 GHz, low cut-off: 2.6 GHz). A short section of reduced intensity noise is noticeable in both sweeping directions, giving strong indications of sweet spot operation [41,55,56]. As mentioned above, minimizing the chromatic dispersion further improves sweet spot operation by reducing the number of intensity dips [39,41,43,55–57]. However, a clear, visible sweet spot is necessary to measure and compensate residual dispersion very accurately, which is more challenging to achieve here due to high losses, lower gain, and low COD threshold of the SOA_1. Due to the low COD, the gain in the laser is limited to a driving current of ~ 160 mA out of a maximum of 250 mA. The steep edge in the center of both sweeps, where the noise abruptly decreases, stays low for some time and is again followed by a higher noise region (Fig. 4, red box), can be explained by the fact that noise in FDML lasers with sweet spot operation is governed by the linewidth enhancement factor which is a nonlinear effect [58]. When adjusting the frequency of the laser hertz by hertz to locate the best sweet spot, the steep edge will follow step by step until the frequency is too distorted to detect any reduced intensity noise. For instance, if increasing the frequency by one hertz, the edge will move one step towards longer wavelengths if a forward sweep is considered. This behavior can be used to precisely determine remaining intra-cavity dispersion. The forward and backward sweeps are similar in noise and power.

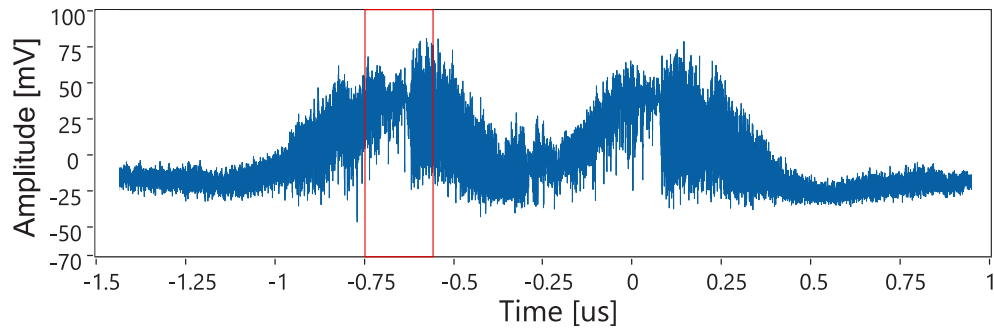


Fig. 4. Amplitude of the noise for both sweeping directions (forward on the left and backward on the right) at the direct output of the FDML laser.

The boosted output of the FDML has an output power of 17 mW, a tuning bandwidth of 40 nm, and the coherence is sufficient for an OCT imaging range of 7 mm at -6 dB sensitivity roll off. The imaging process is described in detail in section 3. Since FDML lasers have a bidirectional sweep operation due to the sinusoidal drive of the FFP-TF as shown in Fig. 4, both sweeps can be used for imaging due to their high similarity. A repetition rate of 828 kHz is then possible and used in the next section.

3. Imaging

3.1. OCT set-up

In Fig. 5, a schematic diagram of the OCT instrument equipped with our FDML source is depicted. Light from the FDML laser is directed toward an 80/20 fiber directional coupler, where 20% of the optical power is conveyed toward the sample arm. The light is then coupled to free space using a fiber collimator (F220APC-850, Thorlabs). It is deflected by two galvanometer scanner mirrors (Cambridge Technology, 6210 H) and directed towards a telescope whose output is a 1.5 mm diameter collimated beam. The other 80% of the light is directed towards the reference arm of the interferometer. The splitting ratio of the coupler ensures a safe power level on the retina while more efficient collection of light from the sample, i.e. 80%. The backscattered light from the sample and reference arm interfering at the 50/50 coupler is detected by a custom-designed balanced silicon photodetector from Wieserlabs. Each photodiode has a responsivity estimated to be 0.33 A/W at 850 nm. The balanced photodetector has an electronic bandwidth of 600 MHz. A 12-bit waveform digitizer board then acquires the signals at a rate of 4 GS/s (AlazarTech, ATS9373) before using the complex master-slave (CMS) procedure to generate images [59,60]. For calibration purposes (computation of the functions describing the unbalanced dispersion in the interferometer as well as the sweeping non-linearity), a model eye including a 19 mm focal length lens (AC127-019-B-ML, Thorlabs) and a flat metallic mirror was employed. The optics of the sample arm are mounted on a motorized stage enabling pupil tracking using two cameras. The length of the sample arm can be adjusted via the computerized stage to change the focal point through the layers of the retina.

All channel spectra (cropped interference signal) must be mathematically transformed ahead to obtain every A-Scan. For this purpose data must be resampled and reorganized if a Fourier transform is used. Instead, the photo-detected signal is processed employing the CMS method. At a calibration stage (Master), using a mirror as a sample, several channeled spectra are acquired for different OPD values. A minimum of two is necessary, in the experiment here, five are acquired sequentially equidistant of 0.5 mm in OPD, starting from ~ 0.5 mm. Based on the protocol described in [59–61], the five channeled spectra allow inferring two functions, g and h , responsible

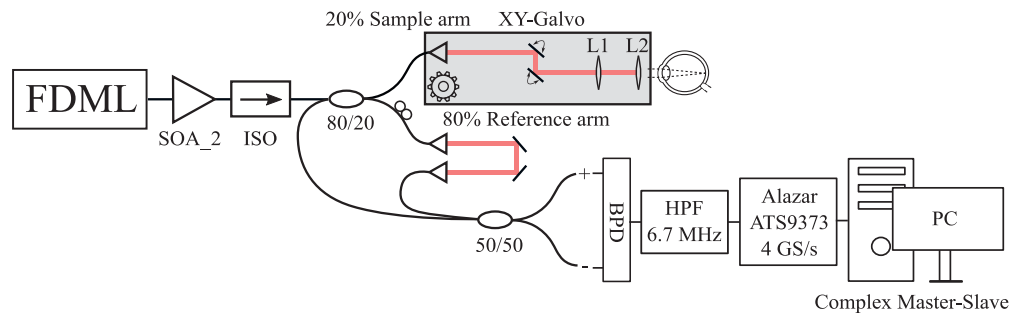


Fig. 5. Schematic of the imaging set-up. The light at the output of the booster enters the sample and reference arms, which are recombined by a 50/50 coupler. BPD: balanced photodetectors, HPF: high pass filter.

for the sweep non-linearities and unbalanced dispersion in the OCT set-up, respectively. Once g and h are known, equivalent complex channeled spectra are calculated for each OPD of interest, called masks and placed in memory. At the measurement stage (Slave), the sample (the eye) replaced the mirror and the acquired channeled spectrum (CS) obtained is multiplied with the set of masks, $M_i(k)$ from the memory:

$$A(z_i) = \sum_{k=k_{min}}^{k_{max}} CS(k)M_i(k) \quad (1)$$

The results are integrated over the wavenumber k and each multiplication delivers the amplitude of the A-scan for the value of each OPD associated to each mask. Due to temperature instabilities, the inference of functions g and h had to be repeated several times to avoid any laser drift during the measurement that would influence g and h and thus, the image quality and resolution. The laser is not thermally insulated so the frequency has to be readjusted occasionally to maintain sweet spot operation [41].

3.2. Laser performance

The sensitivity of the interferometer driven by the FDML was measured with different reference arm power levels that show a plateau at 84.6 dB around 200 μ W as demonstrated in Fig. 6. This plateau (instead of a distinct maximum) indicates shot noise limited performance as explained in [62]. The calculation following [14] gives a theoretical sensitivity of 86.9 dB, with a responsivity of our silicon detector at 850 nm of 0.3 A/W and a power on the sample of 1.2 mW, which was the value used for imaging. The 2.3 dB difference between our measured sensitivity value and the theoretical sensitivity might be due to deviations in the spectral shape, inaccurate power measurements, inaccuracy in the assumed analog detection bandwidth, or other parasitic effects. The maximum permissible exposure (MPE) value for a stationary, collimated beam on the cornea calculated using IEC 60825-1 and ANSI 136.1 is 0.8 mW for 840 nm [63,64]; however this is considering a non-scanning system. Due to continuous scanning without interruptions during an examination, the retina can be exposed with a higher average power of 1.2 mW [65].

The phase stability of the laser has been measured over 1,000 consecutive forward channeled spectra in a common path configuration using a glass plate thickness of 235 μ m introduced halfway through in the reference path, as presented in Ref. [66]. Two different glass thicknesses are used before the measurement to create the masks used for signal processing [59,60]. A 20 GHz oscilloscope (Lecroy Teledyne, Wavemaster 820Zi-b) was used to acquire 1,000 sweeps with 80 GS/s in a single shot. A trigger phase-locked with the filter of the FDML is saved in the meantime and used in post-processing to separate each sweep. Such a strategy is employed

here to avoid a jitter noise that the trigger from the acquisition card could generate. Once all forward sweeps are cropped, the CMS protocol is performed, the interference noise is removed, and an iFFT is used to obtain the linearized signal. The phase is then computed using a Hilbert transform (Fig. 7 (A)). The standard deviation of each point over the sweep is calculated following the method in [66]. As shown in Fig. 7 (B), the laser has an average standard deviation of 14 mrad over 1,000 sweeps. Due to an optimization of the filter frequency to approach sweet spot operation in the middle of the sweep, the phase instability is lower in this region.

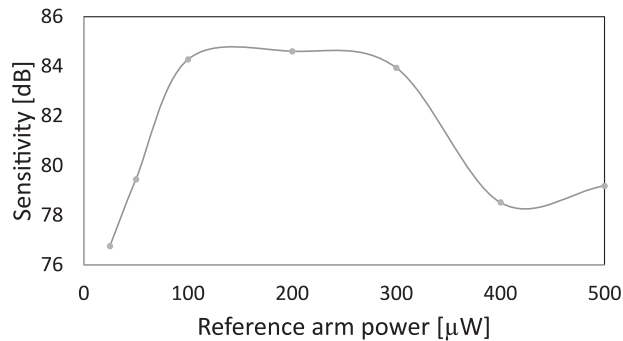


Fig. 6. Sensitivity of the laser measured with different reference arm power levels.

Figure 7 (C) presents the superposition of the phase evolution, expressed by g , along the forward and backward sweep. For both curves, coefficients of determination obtained by using linear fits are above 0.9983. These coefficients could easily increase towards 1.0 by modulating the laser and selecting a narrower, more linear part of the driving signal of the FFP-TF. The g functions are being compared, and the results are shown in Fig. 7 (D). It is clear that both sweeps can be used for imaging due to their similar power level and phase behavior; however, for correct imaging in depth, separate masks need to be employed on each sweep. As a demonstration, Fig. 7 (E) shows A-scans in which correct masks are used for two forward sweeps, where good axial resolution is achieved, as well as forward masks employed for two backward sweeps, leading to a degradation in terms of axial resolution and height of the peaks.

Axial and lateral resolution have been measured and compared with theoretical values. The axial resolution was experimentally measured when imaging the model eye. 7 B-Scans are acquired by altering the length of the reference arm by 0.5 mm OPD between each. Data processing was mapped from linear scale to grey scale. Figure 8 shows all peaks at different depths and a Gaussian fit of the first and last one that gives an evolution of the axial resolution from 12.8 μ m to 12.5 μ m. An average of 13.16 μ m for all peaks is obtained over the entire range. The calculation gives an axial resolution of 10.58 μ m in the air for a top-hat optical spectral shape around 840 ± 20 nm following [67]. The difference of ~ 2.5 μ m comes from the fact that a Hanning window is used in the data processing, which will worsen the axial resolution. A lateral resolution of 17.54 μ m was measured by imaging a 1951 USAF Resolution Target (Thorlabs, R1DS1P), with a fast scanner at 500 Hz driven by a triangular signal of 0.3 V amplitude and a slow scanner at 2.5 Hz as a sawtooth, 0.2 V amplitude. Please note that this measurement does not fully account for the lateral resolution achievable on the retina by eye lens aberrations in the eye.

3.3. Imaging

Retinal images acquired with our 840 nm FDML laser are presented here; all imaging settings are shown in Table 1. All images were acquired on the same healthy volunteer with an optical power of 1.2 mW at the cornea. All imaging experiments were performed at the University of Kent,

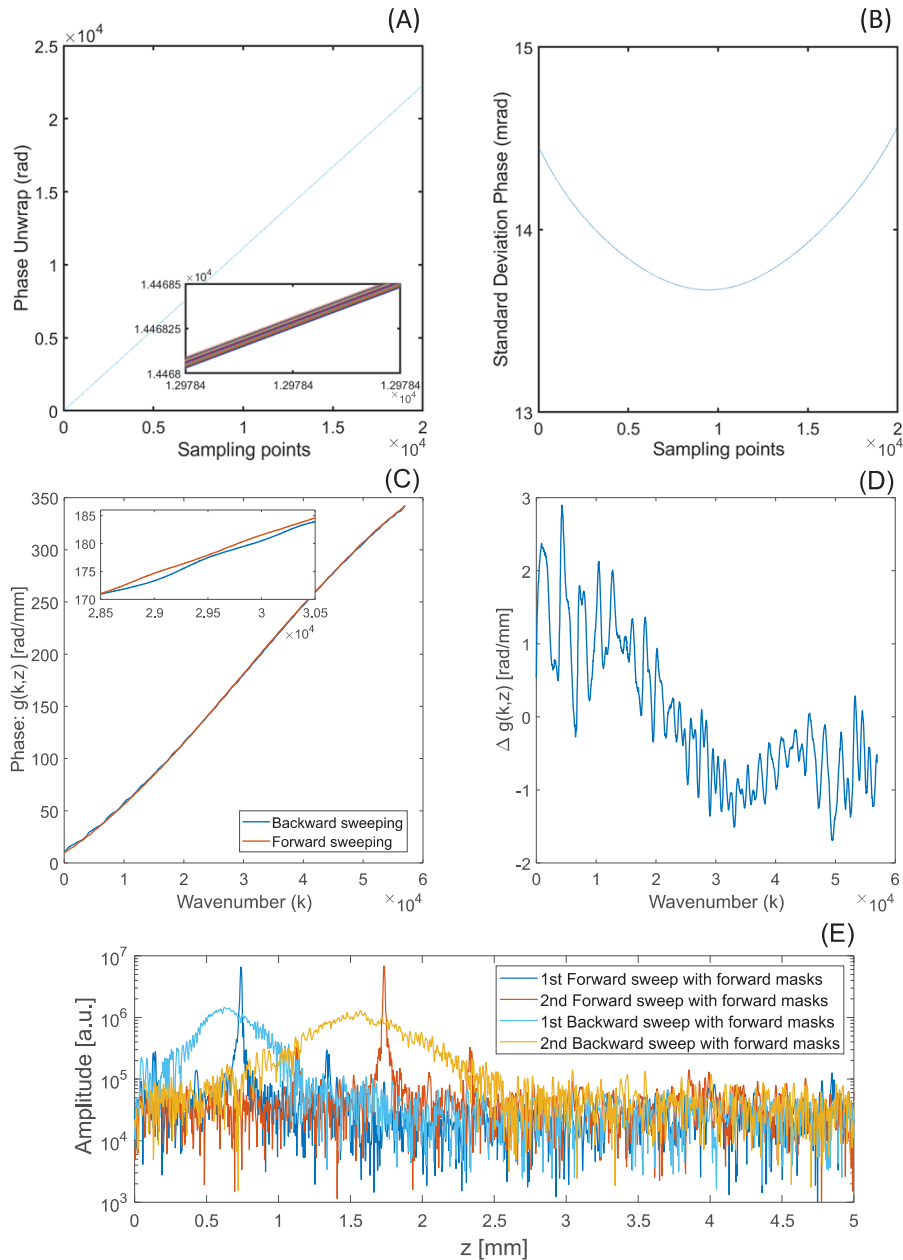


Fig. 7. Phase stability of the laser. (A) Spectral phase for 1,000 forward sweeps, inset: zoom into its fluctuation. (B) Standard deviation for variation of phase among all 1,000 sweeps. (C) comparison of the phase obtained from the g matrix, used for recalibration of the forward and backward sweep. (D) shows the g variation between the forward and backward sweep phases in (C). (E) Four A-Scans were acquired using either a forward or a backward laser sweep. Each A-Scans acquired with a backward sweep have been multiplied with a theoretical forward mask, while each A-Scans acquired with a forward sweep have been multiplied with the right mask (i.e., theoretical forward masks).

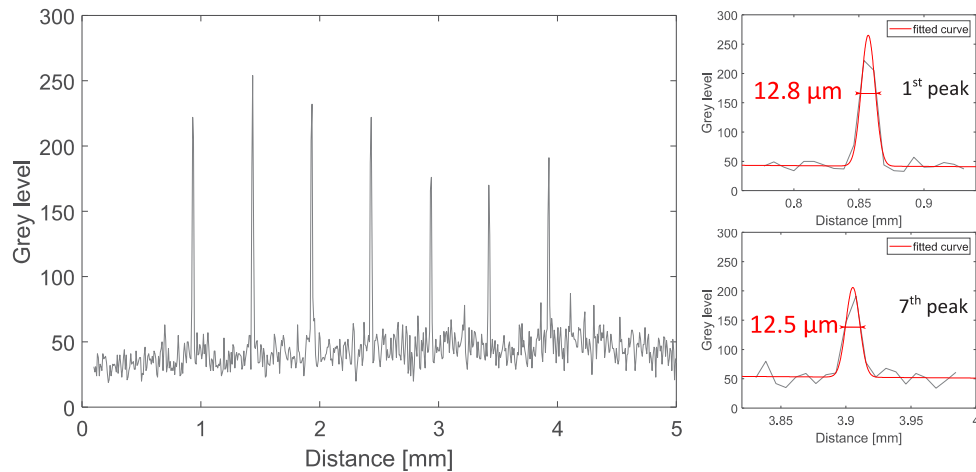


Fig. 8. Axial resolution measured for 7 different depths, showing a quasi-constant ~ 12.8 μm resolution over the range.

where the ethical approval to image the human retina in-vivo was obtained. Two galvanometer scanners are used to acquire B-scans and volumes (set-up in Fig. 5).

Figure 9 shows the macula region of the subject acquired using the unidirectional forward sweeping of the FDML laser, which corresponds to a rate of 414,000 axial scans per second. The fast lateral scanner (along the horizontal) was driven at 200 Hz, with an amplitude of 2 V, yielding a field of view of 12 mm with 1,000 points. An oversampling factor of ~ 2 is obtained since the lateral resolution of the system is estimated to be 24 μm . 20 consecutive frames have been used for averaging in (A) and 5 in (C). All three brighter layers under the external limiting membrane are visible in the non-averaged image (B). Although the layers are distinguishable without averaging, a 20 times average helps to obtain a better contrast on the ganglion cell layer from the inner plexiform layer and to see the external limiting membrane, as shown in Fig. 9 (A).

Table 1. Acquisition settings of the OCT setup used for each presented figure. FOV: field of view.

Fig. n°	Sweep acquisition	Oversampling	X-Y scanners setting		
			Frequency	FOV	Volume rate
Figure 9. (A-B-C)	Unidirectional	2	200 Hz	12 mm	n/a
Figure 10. (A-B)	Unidirectional	1.6	200 Hz	15.5 mm	n/a
Figure 10. (C-D)	Bidirectional	1	800 Hz	12 mm	n/a
Figure 11. (A)	Unidirectional	2	200 Hz	7.8 mm	1 Hz
Figure 11. (B)	Unidirectional	1	1 kHz	5 mm	10 Hz
Figure 11. (C)	Unidirectional	5	200 Hz	3.2 mm	1 Hz
Figure 11. (D)	Unidirectional	2.5	500 Hz	4 mm	1 Hz

Wider B-Scans have been acquired by increasing the galvanometer scanner amplitude to 3 V at a frequency of 200 Hz, the oversampling decreased to 1.6, and the acquisition time is 5 ms. The fovea and the optic nerve now fit within the same B-Scan image, as shown in Fig. 10. Figure 10 (B) is an unaveraged frame of the averaged image stack in (A). The three brighter layers under the external limiting membrane can again be appreciated, as well as the choroid. Figure 10 (C) and (D) are acquired using the bidirectional sweeping of the filter, which corresponds to 2×414 kHz, resulting in an A-Scan rate of 828,000 per second. All layers depicted in the previous imaging

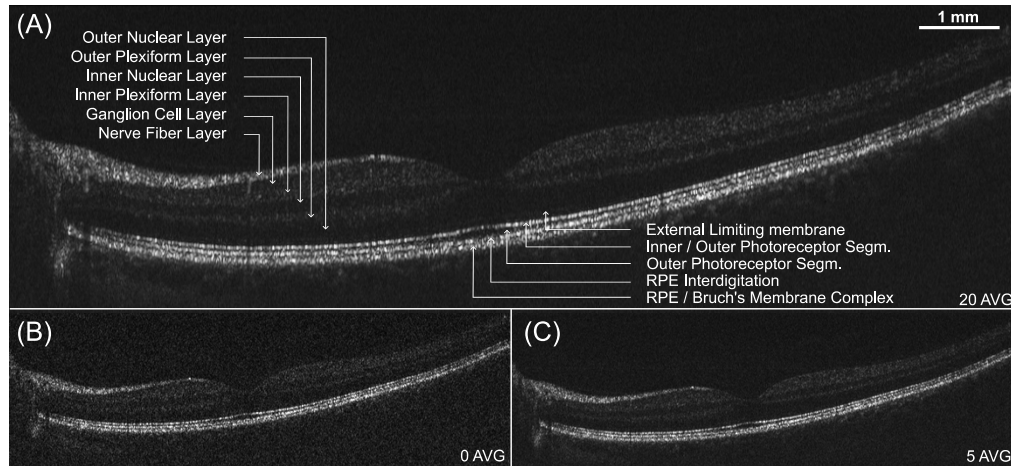


Fig. 9. Retinal OCT imaging focused on the macula. (A) is 20 times averaged, (B) is obtained without average, and (C) is 5 times averaged. RPE: retinal pigment epithelium.

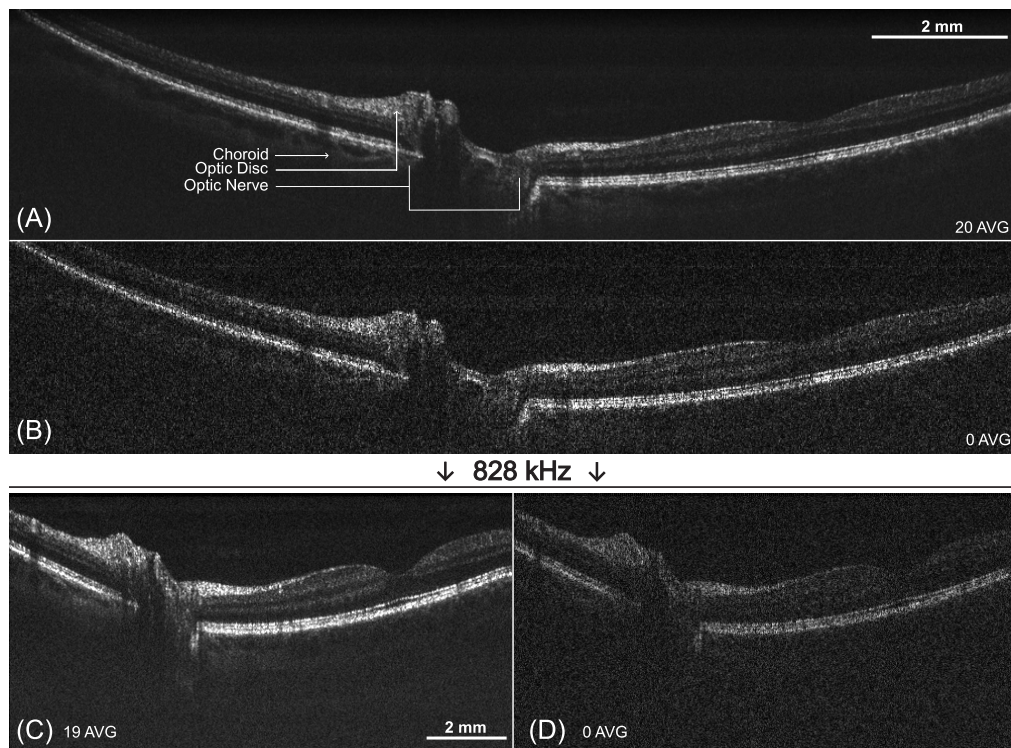


Fig. 10. Widefield retinal images of the optic nerve and the fovea. (A) and (B) are acquired at a rate of 414,000 axial scans per second, 20 times average and non-average, respectively. (C) and (D) are acquired using the laser's bidirectional sweeping, leading to a rate of 818,000 axial scans per second. (C) is 19 times averaged, and (D) is non-averaged.

can still be seen at this higher repetition rate. However, as mentioned in section 3.2, two sets of g and h were used, one for each sweep. This led to a slight frequency shift between the forward and backward A-scan. A correction of 3 pixels is applied to each backward sweep, leading to the images (D) in Fig. 10. Image correction has such a small impact on the visibility of layers that it is not discernible.

En-face OCT aggregated *en-face*, similar to confocal or fundus images and 3D images, are presented in Fig. 11. The fundus images are obtained by superposing all *en-face* OCT images together for all masks [68]. In (A), an average of 8 such equivalent confocal images show the optic nerve and the macula. Each of the 8 volumes took 1 s, and the fast and slow scanners were driven at 200 Hz (triangular) and 1 Hz (sawtooth) frequency, respectively. The CMS approach employed here allowed for *en-face* OCT and confocal images to be displayed in real-time. For instance, Fig. 11 (B) has been acquired in 100 ms. The volume (B) and (D) have been flattened in post-processing for a better rendering. They are presented with three *en-face* images separated each by 10 frames. In each image, vessels can be seen, as well as smaller capillaries.

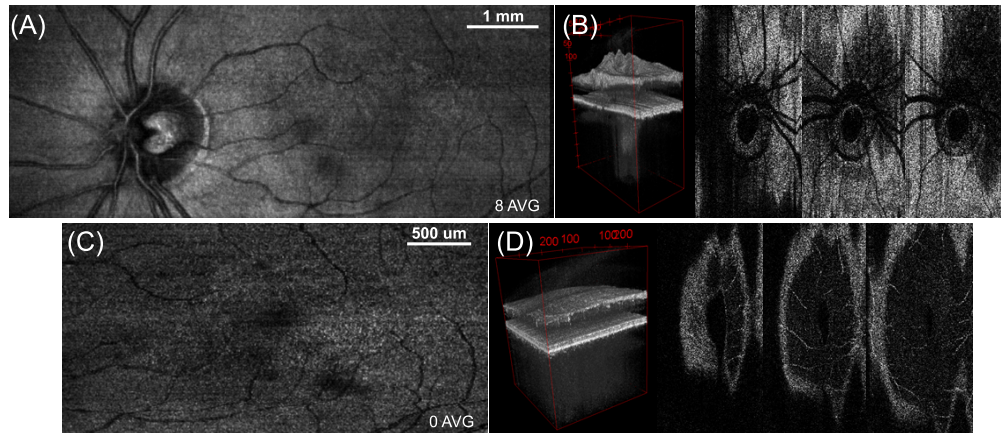


Fig. 11. *En-face* OCT and confocal images of the optic nerve and the macula regions acquired at a rate of 414,000 axial scans per second. (A) 8 times averaging of confocal images of the optic nerve and the macula. (B) flattened 3D of the optic nerve with 3 corresponding *en-face* spaced by 10 frames. (C) confocal images of the macula. (D) flattened 3D of the macula with 3 corresponding *en-face* spaced by 10 frames.

4. Conclusion

In this work, we demonstrated an 840 nm FDML laser whose performance was demonstrated by imaging the human eye. Bidirectional sweeping was used to acquire images at a rate of 828,000 axial scans per second. Thanks to a tuning bandwidth of 40 nm, an axial resolution in water of 9.89 μm is achieved, enabling decent distinction of retinal layers in depth. The sensitivity of 84.6 dB might limit the quality of the image compared to images achieved with a 1060 nm FDML laser reaching ~ 90 dB sensitivity [69]. However, most of the layers of interest are already discernible. A long roll off length of the point spread function can be achieved if the source has low intrinsic noise. This indicates good “instantaneous” coherence length. 1300 nm research FDML laser devices have already proven > 10 cm sensitivity roll-off at -6 dB [37]. We achieved with our new source a roll-off of 1.4 cm, which is more than sufficient for retinal imaging, but it might not be sufficient for full eye length measurement. The roll-off of the laser might be improved in the future by even more accurate dispersion compensation in the laser cavity. Also, a higher small signal gain SOA might improve the performance with respect to the spectral

sweep bandwidth and it would decrease the overall noise of the laser. The phase stability of the laser having a standard deviation of time jitter of 25 ps over 1,000 sweeps makes it usable for phase-resolved techniques, such as OCT angiography [70], which has already been shown with a 1060 nm FDML laser in [71]. A stable lateral phase during volume acquisition could be obtained by optical buffering and reach megahertz repetition rate. This will be of interest for opto-retinography [72,73], or will enable aberration correction less affected by movements like in holography [74]. We experienced that the CMS method might be more robust against amplitude noise in the calibration trace than the phase extraction based on Hilbert transform. Also due to the acquisition of several recalibration traces at different depths in CMS, the concept might be more independent of timing miscalibration and phase rotation of the electronics. We also have demonstrated the benefits of using an FDML laser in conjunction with the CMS method, with two main aspects; first, due to the high sweep to sweep stability of the FDML laser, k-clocking is not necessary, and bidirectional sweeping can be achieved after acquiring calibration traces for only one forward and one backward sweep. This makes potential future overall systems costs much more affordable since the super high-speed analog to digital converter is a major cost factor. Secondly, the depth selection enabled by CMS is highly efficient in producing real-time *en-face* images at low computational cost.

Funding. H2020 Marie Skłodowska-Curie Actions (ITN-NETLAS 860807); Deutsche Forschungsgemeinschaft (EXC 2167-390884018); Excellence Chair Program by the universities of Kiel and Luebeck.

Acknowledgments. We gratefully acknowledge Dr. Vladimir Shidlovski for his scientific contribution and help using Superlum Ltd. devices. We acknowledge financial support by Land Schleswig-Holstein within the funding program Open Access Publikationsfonds. Prof. Adrian Podoleanu further acknowledges the NIHR (BRC4-05-RB413-302) at the UCL, Institute of ophthalmology and BBSRC (BB/S0166431). Dr. Adrian Bradu acknowledges the support of the Royal Society, project PARSOCT, RGS/R1/221324 and the support of the Academy of Medical Sciences/the Wellcome Trust/the Government Department of Business, Energy and Industrial Strategy/the British Heart Foundation/ Diabetes UK Spring-board Award SBF007\100162.

Disclosures. T. Pfeiffer: University of Lübeck (P), Optores GmbH (E); A. Mlynek: Optores GmbH (E); W. Wieser: Ludwig Maximilian University of Munich (P), Optores GmbH (I, E); A. Chamorovskiy: Superlum Ltd. (E); A. Bradu: University of Kent (P); A. Podoleanu: University of Kent (P); R. Huber: University of Lübeck (P), Ludwig Maximilian University of Munich (P), Optores GmbH (I, P, R), Optovue Inc. (I, R), Abott (I, R).

Data Availability. Data underlying the results presented in this paper are not publicly available at this time but may be obtained from the authors upon reasonable request.

References

1. W. Drexler, U. Morgner, R. K. Ghanta, F. X. Kärtner, J. S. Schuman, and J. G. Fujimoto, "Ultrahigh-resolution ophthalmic optical coherence tomography," *Nat. Med.* **7**(4), 502–507 (2001).
2. M. Everett, S. Magazzeni, T. Schmoll, and M. Kempe, "Optical coherence tomography: From technology to applications in ophthalmology," *Transl. Biophotonics* **3**(1), e202000012 (2021).
3. L. An, P. Li, G. Lan, D. Malchow, and R. K. Wang, "High-resolution 1050 nm spectral domain retinal optical coherence tomography at 120 kHz A-scan rate with 6.1 mm imaging depth," *Biomed. Opt. Express* **4**(2), 245–259 (2013).
4. J. F. Bille, *High Resolution Imaging in Microscopy and Ophthalmology: New Frontiers in Biomedical Optics*, J. F. Bille, ed., (Springer, 2019).
5. J. Reche, A. Stocker, V. Henchoz, O. Habra, P. Escher, S. Wolf, and M. Zinkernagel, "High-resolution optical coherence tomography in healthy individuals provides resolution at the cellular and subcellular levels," *Trans. Vis. Sci. Tech.* **12**(7), 12 (2023).
6. P. J. Rosenfeld, M. K. Durbin, L. Roisman, F. Zheng, A. Miller, G. Robbins, K. B. Schaal, and G. Gregori, "ZEISS Angioplex™ Spectral Domain Optical Coherence Tomography Angiography: Technical Aspects," in *OCT Angiography in Retinal and Macular Diseases*, p. 0, S. Karger AG (2016).
7. O. P. Kocaoglu, T. L. Turner, Z. Liu, and D. T. Miller, "Adaptive optics optical coherence tomography at 1 MHz," *Biomed. Opt. Express* **5**(12), 4186–4200 (2014).
8. D. Valente, K. V. Vienola, R. J. Zawadzki, and R. S. Jonnal, "Kilohertz retinal FF-SS-OCT and flood imaging with hardware-based adaptive optics," *Biomed. Opt. Express* **11**(10), 5995–6011 (2020).
9. B. Karamata, M. Laubscher, M. Leutenegger, S. Bourquin, T. Lasser, and P. Lambelet, "Multiple scattering in optical coherence tomography. I. Investigation and modeling," *J. Opt. Soc. Am. A* **22**(7), 1369–1379 (2005).
10. P. Stremplewski, E. Auksoorius, P. Wnuk, Ł. Kozon, P. Garstecki, and M. Wojtkowski, "In vivo volumetric imaging by crosstalk-free full-field OCT," *Optica* **6**(5), 608–617 (2019).

11. A. M. Jiménez, S. Grelet, V. Tsaturian, P. B. Montague, A. Bradu, and A. Podoleanu, "400 Hz volume rate swept-source optical coherence tomography at 1060 nm using a KTN deflector," *IEEE Photonics Technol. Lett.* **34**(23), 1277–1280 (2022).
12. J. P. Kolb, T. Klein, W. Wieser, W. Draxinger, and R. Huber, "Full volumetric video rate OCT of the posterior eye with up to 195.2 volumes/s," *Proc. SPIE* **9312**, 931202 (2015).
13. T. Klein, W. Wieser, C. M. Eigenwillig, B. R. Biedermann, and R. Huber, "Megahertz OCT for ultrawide-field retinal imaging with a 1050 nm Fourier domain mode-locked laser," *Opt. Express* **19**(4), 3044–3062 (2011).
14. T. Klein, W. Wieser, L. Reznicek, A. Neubauer, A. Kampik, and R. Huber, "Multi-MHz retinal OCT," *Biomed. Opt. Express* **4**(10), 1890–1908 (2013).
15. J. P. Kolb, T. Klein, C. L. Kufner, W. Wieser, A. S. Neubauer, and R. Huber, "Ultra-widefield retinal MHz-OCT imaging with up to 100 degrees viewing angle," *Biomed. Opt. Express* **6**(5), 1534–1552 (2015).
16. L. Reznicek, J. P. Kolb, T. Klein, K. J. Mohler, W. Wieser, R. Huber, M. Kernt, J. März, and A. S. Neubauer, "Wide-field megahertz OCT imaging of patients with diabetic retinopathy," *J. Diabetes Res.* **2015**, 1–5 (2015).
17. S. Marschall, C. Pedersen, and P. E. Andersen, "Investigation of the impact of water absorption on retinal OCT imaging in the 1060 nm range," *Biomed. Opt. Express* **3**(7), 1620–1631 (2012).
18. B. Povazay, B. M. Hermann, A. Unterhuber, B. Hofer, H. Stattmann, F. Zeiler, J. E. Morgan, C. Falkner-Radler, C. Glittenberg, S. Binder, and W. Drexler, "Three-dimensional optical coherence tomography at 1050 nm versus 800 nm in retinal pathologies: enhanced performance and choroidal penetration in cataract patients," *J. Biomed. Opt.* **12**(4), 041211 (2007).
19. S. Hariri, A. A. Moayed, A. Dracopoulos, C. Hyun, S. Boyd, and K. Bizheva, "Limiting factors to the OCT axial resolution for in-vivo imaging of human and rodent retina in the 1060 nm wavelength range," *Opt. Express* **17**(26), 24304–24316 (2009).
20. J. P. Kolb, T. Klein, M. Eibl, T. Pfeiffer, W. Wieser, and R. Huber, "Megahertz FDML laser with up to 143 nm sweep range for ultrahigh resolution OCT at 1050 nm," *Proc. SPIE* **9697**, 969703 (2016).
21. W. Drexler, "Ultrahigh-resolution optical coherence tomography," *J. Biomed. Opt.* **9**(1), 47–74 (2004).
22. N. A. Nassif, B. Cense, B. H. Park, M. C. Pierce, S. H. Yun, B. E. Bouma, G. J. Tearney, T. C. Chen, and J. F. D. Boer, "In vivo high-resolution video-rate spectral-domain optical coherence tomography of the human retina and optic nerve," *Opt. Express* **12**(3), 367–376 (2004).
23. E. A. Rank, S. Nevlacsil, P. Muellner, R. Hainberger, M. Salas, S. Gloor, M. Duell, M. Sagmeister, J. Kraft, R. A. Leitgeb, and W. Drexler, "In vivo human retinal swept source optical coherence tomography and angiography at 830 nm with a CMOS compatible photonic integrated circuit," *Sci. Rep.* **11**(1), 21052 (2021).
24. M. Wojtkowski, R. Leitgeb, A. Kowalczyk, T. Bajraszewski, and A. F. Fercher, "In vivo human retinal imaging by Fourier domain optical coherence tomography," *J. Biomed. Opt.* **7**(3), 457–463 (2002).
25. Y. Chen, D. L. Burnes, M. D. de Bruin, M. Mujat, and J. F. de Boer, "Three-dimensional pointwise comparison of human retinal optical property at 845 and 1060 nm using optical frequency domain imaging," *J. Biomed. Opt.* **14**(2), 024016 (2009).
26. M. Kendrisic, V. Agafonov, M. Salas, L. Ferrara, M. Niederleithner, H. Resch, S. Steiner, C. Vass, W. Drexler, and R. A. Leitgeb, "Thermally tuned VCSEL at 850 nm as a low-cost alternative source for full-eye SS-OCT," *Opt. Lett.* **48**(11), 3079–3082 (2023).
27. S.-W. Lee, H.-W. Song, B.-K. Kim, M.-Y. Jung, S.-H. Kim, J.-D. Cho, and C.-S. Kim, "Fourier domain optical coherence tomography for retinal imaging with 800-nm swept source: real-time resampling in k-domain," *J. Opt. Soc. Korea* **15**(3), 293–299 (2011).
28. V. J. Srinivasan, R. Huber, I. Gorczynska, J. G. Fujimoto, J. Y. Jiang, P. Reisen, and A. E. Cable, "High-speed, high-resolution optical coherence tomography retinal imaging with a frequency-swept laser at 850 nm," *Opt. Lett.* **32**(4), 361–363 (2007).
29. K. Goda, A. Fard, O. Malik, G. Fu, A. Quach, and B. Jalali, "High-throughput optical coherence tomography at 800 nm," *Opt. Express* **20**(18), 19612–19617 (2012).
30. F. Toadere, R. F. Stancu, W. Poon, D. Schultz, and A. Podoleanu, "1 MHz akinetic dispersive ring cavity swept source at 850 nm," *IEEE Photonics Technol. Lett.* **29**(11), 933–936 (2017).
31. H. A. Davani, C. Grasse, B. Kögel, C. Gierl, K. Zogal, T. Gründl, P. Westbergh, S. Jatta, G. Böhm, P. Meissner, A. Larsson, and M.-C. Amann, "Widely electro thermal tunable bulk-micromachined MEMS-VCSEL operating around 850 nm," *Proceedings of the International Quantum Electronics Conference and Conference on Lasers and Electro-Optics Pacific Rim 2011* C829 (2011).
32. H. A. Davani, C. Grasse, B. Kögel, P. Westbergh, C. Gierl, K. Zogal, S. Jatta, G. Böhm, T. Gründl, P. Meissner, A. Larsson, and M. C. Amann, "Widely tunable high-speed bulk-micromachined short-wavelength MEMS-VCSEL," *22nd IEEE International Semiconductor Laser Conference* 9–10 (2010).
33. D. D. John, B. Lee, B. Potsaid, A. C. Kennedy, M. E. Robertson, C. B. Burgner, A. E. Cable, J. G. Fujimoto, and V. Jayaraman, "Single-Mode and High-Speed 850 nm MEMS-VCSEL," in *OSA Technical Digest (online), Lasers Congress 2016 (ASSL, LSC, LAC) ATH5A.2* (2016).
34. J. Cho, G. Gulsen, and C.-S. Kim, "800-nm-centered swept laser for spectroscopic optical coherence tomography," *Laser Phys.* **24**(4), 045605 (2014).
35. H. Lim, J. F. D. Boer, B. H. Park, E. C. W. Lee, R. Yelin, and S. H. Yun, "Optical frequency domain imaging with a rapidly swept laser in the 815–870 nm range," *Opt. Express* **14**(13), 5937–5944 (2006).

36. M. Strupler, N. Goulamhousen, E. D. Montigny, and C. Boudoux, "Rapidly Wavelength-Swept Laser at 780 nm," *IEEE Photonics Technol. Lett.* **23**(4), 197–199 (2011).
37. M. Göb, T. Pfeiffer, W. Draxinger, S. Lotz, J. P. Kolb, and R. Huber, "Continuous spectral zooming for in vivo live 4D-OCT with MHz A-scan rates and long coherence," *Biomed. Opt. Express* **13**(2), 713–727 (2022).
38. C. Grill, T. Blömker, M. Schmidt, D. Kastner, T. Pfeiffer, J. P. Kolb, W. Draxinger, S. Karpf, C. Jirauschek, and R. Huber, "Towards phase-stabilized Fourier domain mode-locked frequency combs," *Commun. Phys.* **5**(1), 212 (2022).
39. D. C. Adler, W. Wieser, F. Trepanier, J. M. Schmitt, and R. A. Huber, "Extended coherence length Fourier domain mode locked lasers at 1310 nm," *Opt. Express* **19**(21), 20930–20939 (2011).
40. T. Pfeiffer, M. Göb, W. Draxinger, S. Karpf, J. P. Kolb, and R. Huber, "Flexible A-scan rate MHz-OCT: efficient computational downscaling by coherent averaging," *Biomed. Opt. Express* **11**(11), 6799–6811 (2020).
41. T. Pfeiffer, M. Petermann, W. Draxinger, C. Jirauschek, and R. Huber, "Ultra low noise Fourier domain mode locked laser for high quality megahertz optical coherence tomography," *Biomed. Opt. Express* **9**(9), 4130–4148 (2018).
42. M. Schmidt, T. Pfeiffer, C. Grill, R. Huber, and C. Jirauschek, "Self-stabilization mechanism in ultra-stable Fourier domain mode-locked (FDML) lasers," *OSA Continuum* **3**(6), 1589–1607 (2020).
43. W. Wieser, T. Klein, D. C. Adler, F. Trépanier, C. M. Eigenwillig, S. Karpf, J. M. Schmitt, and R. Huber, "Extended coherence length megahertz FDML and its application for anterior segment imaging," *Biomed. Opt. Express* **3**(10), 2647–2657 (2012).
44. R. Huber, M. Wojtkowski, and J. G. Fujimoto, "Fourier Domain Mode Locking (FDML): A new laser operating regime and applications for optical coherence tomography," *Opt. Express* **14**(8), 3225–3237 (2006).
45. W. Wieser, B. R. Biedermann, T. Klein, C. M. Eigenwillig, and R. Huber, "Multi-Megahertz OCT: High quality 3D imaging at 20 million A-scans and 4.5 GVoxels per second," *Opt. Express* **18**(14), 14685–14704 (2010).
46. M. Göb, S. Burhan, S. Lotz, and R. Huber, "Towards ultra-large area vascular contrast skin imaging using multi-MHz-OCT," *Proc. SPIE* **1194**, 1194807 (2022).
47. M. Göb, S. Lotz, L. Ha-Wissel, S. Burhan, S. Böttger, F. Ernst, J. Hundt, and R. Huber, "Large area robotically assisted optical coherence tomography (LARA-OCT) for skin imaging with MHz-OCT surface tracking," *Proc. SPIE* **1236**, 123670C (2023).
48. J. P. Kolb, W. Draxinger, J. Klee, T. Pfeiffer, M. Eibl, T. Klein, W. Wieser, and R. Huber, "Correction: Live video rate volumetric OCT imaging of the retina with multi-MHz A-scan rates," *PLoS One* **14**, e0220829 (2019).
49. H. Hakert, M. Eibl, M. Tillich, R. Pries, G. Hüttmann, R. Brinkmann, B. Wollenberg, K.-L. Bruchhage, S. Karpf, and R. Huber, "Time-encoded stimulated Raman scattering microscopy of tumorous human pharynx tissue in the fingerprint region from 1500–1800 cm⁻¹," *Opt. Lett.* **46**(14), 3456–3459 (2021).
50. S. Burhan, N. Detrez, K. Rewerts, M. Göb, C. Hagem, M. M. Bonsanto, D. Theisen-Kunde, R. Huber, and R. Brinkmann, "Characterization of brain tumor tissue by time-resolved, phase-sensitive optical coherence elastography at 3.2 MHz line rate," *Proc. SPIE* **1236**, 123680F (2023).
51. Y. Jiang, S. Karpf, and B. Jalali, "Time-stretch LiDAR as a spectrally scanned time-of-flight ranging camera," *Nat. Photonics* **14**(1), 14–18 (2020).
52. S. Karpf, C. T. Riche, D. Di Carlo, A. Goel, W. A. Zeiger, A. Suresh, C. Portera-Cailliau, and B. Jalali, "Spectro-temporal encoded multiphoton microscopy and fluorescence lifetime imaging at kilohertz frame-rates," *Nat. Commun.* **11**(1), 2062 (2020).
53. M. Klufits, S. Lotz, M. A. Bashir, T. Pfeiffer, A. Mlynek, W. Wieser, A. Chamorovskiy, V. Shidlovski, and R. Huber, "850 nm FDML: performance and challenges," *Proc. SPIE* **1236**, 1236705 (2023).
54. M. Klufits, S. Lotz, M. Bashir, S. Karpf, and R. Huber, "Ultra-high-accuracy chromatic dispersion measurement in optical fibers," *Proc. SPIE* **1199**, 119970L (2022).
55. T. Kraetschmer and S. T. Sanders, "Ultrastable Fourier Domain Mode Locking Observed in a Laser Sweeping 1363.8–1367.3 nm," in *OSA Technical Digest (CD), Conference on Lasers and Electro-Optics/International Quantum Electronics Conference CFB4* (2009).
56. S. Slepneva, B. Kelleher, B. O'Shaughnessy, S. P. Hegarty, A. G. Vladimirov, and G. Huyet, "Dynamics of Fourier domain mode-locked lasers," *Opt. Express* **21**(16), 19240–19251 (2013).
57. B. R. Biedermann, W. Wieser, C. M. Eigenwillig, T. Klein, and R. Huber, "Dispersion, coherence and noise of Fourier domain mode locked lasers," *Opt. Express* **17**(12), 9947–9961 (2009).
58. Ö. E. Aşırım, R. Huber, and C. Jirauschek, "Influence of the linewidth enhancement factor on the signal pattern of Fourier domain mode-locked lasers," *Appl. Phys. B* **128**(12), 218 (2022).
59. A. Bradu, N. M. Israelsen, M. Maria, M. J. Marques, S. Rivet, T. Feuchter, O. Bang, and A. Podoleanu, "Recovering distance information in spectral domain interferometry," *Sci. Rep.* **8**(1), 15445 (2018).
60. S. Rivet, M. Maria, A. Bradu, T. Feuchter, L. Leick, and A. Podoleanu, "Complex master slave interferometry," *Opt. Express* **24**(3), 2885–2904 (2016).
61. A. G. Podoleanu and A. Bradu, "Master–slave interferometry for parallel spectral domain interferometry sensing and versatile 3D optical coherence tomography," *Opt. Express* **21**(16), 19324–19338 (2013).
62. R. Leitgeb, C. K. Hitzenberger, and A. F. Fercher, "Performance of Fourier domain vs. time domain optical coherence tomography," *Opt. Express* **11**(8), 889–894 (2003).
63. ANSI, "American National Standard for Safe Use of Lasers (ANSI 136.1)," In: *ANSI 136.1–2000*. The Laser Institute of America, Orlando, FL, USA (2000).
64. IEC60825–1, "Safety of laser products – Part 1: Equipment classification and requirements," (2014).

65. L. von der Emde, M. Saßmannshausen, O. Morelle, G. Rennen, F. G. Holz, M. W. M. Wintergerst, and T. Ach, "Reliability of Retinal Layer Annotation with a Novel, High-Resolution Optical Coherence Tomography Device: A Comparative Study," in *Bioengineering* (2023).
66. K. S. Park, E. Park, H. Lee, H.-J. Lee, S.-W. Lee, and T. J. Eom, "Phase stable swept-source optical coherence tomography with active mode-locking laser for contrast enhancements of retinal angiography," *Sci. Rep.* **11**(1), 16636 (2021).
67. J. P. Fingler, "Motion contrast using optical coherence tomography," California Institute of Technology, Ph.D. Thesis (2007).
68. A. Bradu, K. Kapinchev, F. Barnes, and A. Podoleanu, "Master slave en-face OCT/SLO," *Biomed. Opt. Express* **6**(9), 3655–3669 (2015).
69. J. P. Kolb, T. Pfeiffer, M. Eibl, H. Hakert, and R. Huber, "High-resolution retinal swept source optical coherence tomography with an ultra-wideband Fourier-domain mode-locked laser at MHz A-scan rates," *Biomed. Opt. Express* **9**(1), 120–130 (2018).
70. B. Braaf, K. A. Vermeer, V. A. D. P. Sicam, E. van Zeeburg, J. C. van Meurs, and J. F. de Boer, "Phase-stabilized optical frequency domain imaging at 1- μ m for the measurement of blood flow in the human choroid," *Opt. Express* **19**(21), 20886–20903 (2011).
71. Y. Miao, M. Siadati, J. Song, D. Ma, Y. Jian, M. F. Beg, M. V. Sarunic, and M. J. Ju, "Phase-corrected buffer averaging for enhanced OCT angiography using FDML laser," *Opt. Lett.* **46**(16), 3833–3836 (2021).
72. D. Hillmann, H. Spahr, C. Pfäffle, H. Sudkamp, G. Franke, and G. Hüttmann, "In vivo optical imaging of physiological responses to photostimulation in human photoreceptors," *Proc. Natl. Acad. Sci.* **113**(46), 13138–13143 (2016).
73. H. Spahr, D. Hillmann, C. Hain, C. Pfäffle, H. Sudkamp, G. Franke, and G. Hüttmann, "Imaging pulse wave propagation in human retinal vessels using full-field swept-source optical coherence tomography," *Opt. Lett.* **40**(20), 4771–4774 (2015).
74. D. Hillmann, H. Spahr, C. Hain, H. Sudkamp, G. Franke, C. Pfäffle, C. Winter, and G. Hüttmann, "Aberration-free volumetric high-speed imaging of in vivo retina," *Sci. Rep.* **6**(1), 35209 (2016).